

Constraining Extended Gamma-ray Emission from Galaxy Clusters

Jiaxin Han,^{1,2,3*} Carlos S. Frenk,³ Vincent R. Eke,³ Liang Gao,^{4,3}
Simon D. M. White,⁵ Alexey Boyarsky,^{6,7} Denys Malyshev⁷ and Oleg Ruchayskiy⁸

¹Key Laboratory for Research in Galaxies and Cosmology, Shanghai Astronomical Observatory, Shanghai 200030, China

²Graduate School of the Chinese Academy of Sciences, 19A, Yuquan Road, Beijing 100049, China

³Institute of Computational Cosmology, Department of Physics, University of Durham, Science Laboratories, South Road, Durham DH1 3LE

⁴Partner Group of the Max Planck Institute for Astrophysics, National Astronomical Observatories, Chinese Academy of Sciences, Beijing, 100012, China

⁵Max-Planck Institute for Astrophysics, Karl-Schwarzschild Str. 1, D-85748, Garching, Germany

⁶Instituut-Lorentz for Theoretical Physics, Universiteit Leiden, Niels Bohrweg 2, Leiden, The Netherlands

⁷Bogolyubov Institute of Theoretical Physics, Kyiv, Ukraine

⁸CERN Physics Department, Theory Division, CH-1211 Geneva 23, Switzerland

28 July 2018

ABSTRACT

Cold dark matter models predict the existence of a large number of substructures within dark matter halos. If the cold dark matter consists of weakly interacting massive particles, their annihilation within these substructures could lead to diffuse GeV emission that would dominate over the annihilation signal of the host halo. In this work we search for GeV emission from three nearby galaxy clusters: Coma, Virgo and Fornax. We first remove known extragalactic and galactic diffuse gamma-ray backgrounds and point sources from the Fermi 2-year catalog and find a significant residual diffuse emission in all three clusters. We then investigate whether this emission is due to (i) unresolved point sources; (ii) dark matter annihilation; or (iii) cosmic rays (CR). Using 45 months of Fermi-LAT data we detect several new point sources (not present in the Fermi 2-year point source catalogue) which contaminate the signal previously analyzed by Han et al. Including these and accounting for the effects of undetected point sources, we find no significant detection of extended emission from the three clusters studied. Instead, we determine upper limits on emission due to dark matter annihilation and cosmic rays. For Fornax and Virgo the limits on CR emission are consistent with theoretical models, but for Coma the upper limit is a factor of 2 below the theoretical expectation. Allowing for systematic uncertainties associated with the treatment of CR, the upper limits on the cross section for dark matter annihilation from our clusters are more stringent than those from analyses of dwarf galaxies in the Milky Way. Adopting a boost factor of $\sim 10^3$ from subhalos on cluster luminosity as suggested by recent theoretical models, we rule out the thermal cross section for supersymmetric dark matter particles for masses as large as 100 GeV (depending on the annihilation channel).

Key words: dark matter experiments, gamma ray experiments, galaxy clusters

1 INTRODUCTION

The existence of dark matter (DM) in the universe has so far only been deduced from its gravitational effect, due to the lack of electromagnetic interactions of the DM with itself or with baryonic matter. There are several elemen-

tary particle candidates for DM in various extensions of the standard model of particle physics (Bertone et al. 2004). Weakly interacting massive particles or WIMPs (with a self-interaction cross-section at roughly the weak scale) are one class of the popular dark matter candidates. These particles could be related to the electroweak symmetry breaking which is currently being explored by experiments at the LHC. For example, within the framework of the min-

* jxhan@shao.ac.cn

imal supersymmetric standard model (MSSM), the lightest neutralino emerges as a candidate WIMP that is stable over cosmological timescales and can annihilate into standard model particles. WIMPs behave as cold dark matter since their primordial velocity dispersion is negligible. High resolution N-body simulations show that cold dark matter halos contain a population of self-bound substructures (subhalos) whose number decreases with increasing subhalo mass as $N \propto M^{-\alpha}$ with $\alpha \approx 1.9$ (Diemand et al. 2007; Springel et al. 2008; Gao et al. 2012)

Much effort has been devoted to the search for WIMPs either directly or indirectly. Direct detection involves identifying the rare events of DM scattering off ordinary matter or searching for new particles near the weak scale at the LHC. Indirect detection involves looking for the annihilation or decay products of dark matter in cosmic rays and gamma rays. In particular, pair annihilation produces gamma-ray photons at a rate proportional to the square of the dark matter density, which then propagate, almost without absorption, to the observer. In this case, the Galactic centre should be the brightest gamma-ray source on the sky (Springel et al. 2008, and references therein). Extended emission (distinct from the central point source) was reported from the central 1° around the Galactic centre by Hooper & Goodenough (2011); Hooper & Linden (2011b).¹ This emission has been interpreted as a signal from dark matter annihilation. There is, however, a strong ambiguity in modeling this region of the Galaxy. Its angular size is comparable with the PSF size of the Fermi LAT at these energies, and the galactic diffuse background there is known to be complicated and highly non-uniform. In particular, it was demonstrated in Boyarsky et al. (2011) that although an extra diffuse component improves the quality of fit, the radial profile of the “extended emission” is fully consistent with that of known Fermi point sources and therefore the emission could all originate from point sources at the Galactic centre (see also Abazajian & Kaplinghat 2012). An intriguing aspect of a DM explanation for the gamma-ray emission from the Galactic centre is that the inferred particle mass of around 10 GeV is also the mass claimed to be required to explain other data, such as the synchrotron emission from the Milky Way’s radio filament (Linden et al. 2011) and the “WMAP Haze” (Finkbeiner 2004; Hooper et al. 2007; Hooper & Linden 2011a), as well as signals from the direct detection experiments DAMA/LIBRA (Bernabei et al. 2010), CoGeNT (Aalseth et al. 2011b,a) and CRESST-II (Angloher et al. 2012). These signals, however, could be in tension with other direct detection experiments, such as CDMS (Ahmed et al. 2011) and XENON-100 (Aprile et al. 2011), although optimistic arguments also exist (e.g., Collar (2011a,b)). We refer the reader to Hooper (2012) for review.

It has recently been reported that the γ -ray emission from the region around the Galactic centre exhibits a line-like excess at energies ~ 130 GeV (Bringmann et al. 2012; Weniger 2012; Tempel et al. 2012; Su & Finkbeiner 2012). The interpretation of this signal as arising from dark matter particles, however, is controversial (see Boyarsky et al. 2012).

Targeting the entire sky rather than the Galactic centre in searching for annihilation radiation may seem a good strategy since this takes advantage of the large-scale distribution of dark matter while avoiding some of the uncertainties arising from the astrophysical modelling of galactic gamma-ray sources. However, the fact that we are located near the centre of the Galactic halo and that most of the annihilation emission outside the Galactic centre is produced by dark matter substructures (Diemand et al. 2007; Springel et al. 2008) results in a gamma-ray map from annihilation that is almost uniform on large scales. This makes detection within the Milky Way halo a difficult task, exacerbated by the additional uncertainty of having to model the extragalactic background, which is more important on large scales (Zaharijas et al. 2010; Baxter & Dodelson 2011).

Dwarf galaxies are the most DM-dominated objects known, are relatively free from astrophysical contamination and appear compact on the sky. They are therefore promising targets to search for DM annihilation radiation. Recent joint analyses of eight to ten dwarf galaxies (Geringer-Sameth & Koushiappas 2011; Ackermann et al. 2011) resulted in no significant detection but have begun to rule out the canonical annihilation cross-section of $3 \times 10^{-26} \text{ cm}^3 \text{ s}^{-1}$ for DM masses below $\sim 30 - 40$ GeV.

Galaxy clusters are the most massive virialized DM structures in the universe and are also good targets for indirect DM searches. The presence of a large population of DM substructures (or subhalos) predicted by numerical simulations further enhances the detectability of DM in clusters. Although the total mass within subhalos amounts to only 10 to 20 percent of the total halo mass, the density enhancement within subhalos can boost the total cluster annihilation luminosity by a factor as high as 1000 when extrapolated down to a subhalo mass limit of one Earth mass, the fiducial cutoff in the primordial power spectrum of density fluctuations for a typical 100 GeV WIMP (Gao et al. 2012; Pinzke et al. 2011). As the distribution of subhalos is much less concentrated than that of the smooth main halo, the total annihilation emission from clusters is predicted to be extended. Thus, attempts to detect DM annihilation assuming a point source or NFW-squared profile could miss most of the signal. In fact, just such a search using the 11-month Fermi-LAT data has yielded no significant detection of emission from six clusters (Ackermann et al. 2010).

Using the 45-month data, we consider possible contributions from cosmic ray (CR) induced gamma-ray emission and from DM annihilation. For the former (which can be as high as, or higher than the emission from cluster DM annihilation (Jeltema et al. 2009; Pinzke & Pfrommer 2010; Pinzke et al. 2011), we adopt the semi-analytic method developed by Pinzke & Pfrommer (2010). For the later, we adopt the model proposed by Gao et al. (2012) for the cluster DM annihilation profile. We provide constraints on both the CR and DM components for the three galaxy clusters analyzed by Han et al. (2011): Coma, which is predicted to have the highest signal-to-noise according to Gao et al. (2012), and Fornax and Virgo which are predicted to have the lowest astrophysical contamination according to Pinzke et al. (2011).

The current paper replaces an earlier version by a subset of the authors (Han et al. 2012, arXiv:1201.1003). After submission of that version, it was pointed out to us that a

¹ See also a preliminary result by the Fermi-LAT collaboration (Vitale et al. 2009).

number of point sources are present in the full three-year LAT data which were not detected significantly in the data used for the "official" Fermi point source catalogue available at the time of our analysis, the LAT 2-year point source catalogue (2FGL; Nolan et al. (2012)). We now carry out our own point source detection in the regions of interest and find several new point sources.² We account for these new detections in our analysis, as well as for the fact that a significant part of the "smooth" extragalactic background is contributed by point sources below the detection threshold; this alters the noise properties of this background. Both changes reduce the significance of the diffuse components apparently detected in the first version of our paper, so that we can now reliably only place upper limits.

Huang et al. (2012) have recently reported a failure to detect significant DM annihilation emission from a combined analysis of eight galaxy clusters. Our work differs from theirs in several respects: firstly, we assume a DM annihilation profile based on high resolution cosmological simulations (Gao et al. 2012); secondly, we assess the impact of cosmic rays in the detection of dark matter; and finally, we include in our sample the Virgo cluster which turns out to be the best candidate. The constraints we set on the annihilation cross-section are consistent with those of Huang et al. (2012).

The paper is organized as follows. In section 1 we describe the data and provide an overview of the models of the Virgo, Fornax and Coma galaxy clusters regions used in the analysis (see Table 1). The specification of the non-standard components of the models (dark matter and cosmic rays brightness profiles) is provided in Sec. 2. The constraints on CR emission and DM annihilation that we obtain are summarized in section 3 and discussed in Sec. 4.

The cosmological parameters used in this work are the same as those assumed by Gao et al. (2012): $\Omega_m = 0.25$, $\Omega_\Lambda = 0.75$, $h = 0.73$.

1.1 Data preparation

We analyze the first 45 months of data (04/08/2008 to 20/05/2012) from the Fermi-LAT,³ trimmed with the cuts listed below, to select high quality photon events. This typically results in $\sim 10^5$ photons within a radius of 10 degrees around each cluster, while the expected number of annihilation photons is of the order of 10^2 according to Fig. 3. The most recent instrument response function (IRF), P7CLEAN_V6, is adopted for the analysis, in accordance with our event class selection.⁴ The resulting gamma-ray images for the three clusters are shown in the left panel of Fig. 1 for Virgo and in Fig. C1 for Coma and Fornax.

Minimum Energy	100 MeV
Maximum Energy	100 GeV

² We notice that several new point sources in Virgo are also identified in a concurrent paper (Macías-Ramírez et al. 2012) and are found to reduce the significance of DM-like emission in the cluster, consistent with what we find here.

³ <http://fermi.gsfc.nasa.gov/cgi-bin/ssc/LAT/LATDataQuery.cgi>

⁴ We also tried using P7SOURCE_V6 IRF and Event Class 2 data. The results are consistent with those presented in this paper.

Maximum zenith angle ⁵	100 degrees
Event Class ⁶	3 (P7CLEAN)
DATA-QUAL ⁷	1
LAT CONFIG ⁸	1
ABS (ROCK ANGLE) ⁹	< 52 degrees
ROI-based zenith angle cut	yes

We list the basic properties of the three clusters in Table 1.

1.2 Maximum-likelihood fitting

We use the `pyLikelihood` tool shipped with the Fermi Science Tools software package (version v9r27p1-fssc-20120410) to perform a maximum likelihood (ML) analysis (Mattox et al. 1996). After applying appropriate data cuts, as described in section 1.1, we bin the data into 0.1 degree-wide pixels and 30 logarithmic energy bins within a radius of 10 degrees around each cluster. This large radius is chosen to account for the large LAT PSF size at low energies ($4 \sim 10$ degrees at 100 MeV¹⁰). An exposure cube is computed around each cluster covering 25 degrees in radius and the 30 energy bins, using the `gtexpcube2` tool.

In the standard Fermi likelihood analysis, the photon counts within each pixel are treated assuming Poisson statistics for each energy bin to calculate the likelihood. The best-fit parameters are obtained when the likelihood for the entire data set is maximized. The significance of a given component of interest (e.g. DM or CR) from the ML fitting is quantified by the likelihood ratio statistic,

$$TS = -2 \ln(L_0/L), \quad (1)$$

where L is the maximum likelihood for the full model and L_0 is the maximum likelihood for the null hypothesis, i.e. the model *without* the component of interest. According to Wilk's theorem, this test statistic, TS , approximately follows a χ^2 distribution when the null hypothesis is true, with one degree of freedom for our case where the normalization is the only extra parameter in the alternative model. The probability that a given value of TS arises purely from fluctuations of the null hypothesis is:

$$P = \int_{TS}^{\infty} \frac{1}{2} \chi_1^2(\xi) d\xi = \int_{\sqrt{TS}}^{\infty} \frac{e^{-x^2/2}}{\sqrt{2\pi}} dx. \quad (2)$$

⁵ ZENITH ANGLE (degrees): angle between the reconstructed event direction and the zenith line (originates at the centre of the Earth and passes through the centre of mass of the spacecraft, pointing outward). The Earth's limb lies at a zenith angle of 113 degrees.

⁶ EVENT CLASS: flag indicating the probability of the event being a photon and the quality of the event reconstruction.

⁷ DATA-QUAL: flag indicating the quality of the LAT data, where 1 = OK, 2 = waiting review, 3 = good with bad parts, 0 = bad

⁸ LAT-CONFIG: flag for the configuration of the lat (1 = nominal science configuration, 0 = not recommended for analysis)

⁹ ROCK ANGLE: angle of the spacecraft z -axis from the zenith (positive values indicate a rock toward the north).

¹⁰ The LAT PSF size scales roughly as $E^{-0.8}$, so at 1 GeV it is ~ 1 deg

Table 1. Basic Properties of Target Clusters

	Coma	Fornax	Virgo (M87)
RA (deg)	194.9468	54.6686	187.6958
DEC (deg)	27.9388	-35.3103	12.3369
D_A (Mpc) ^a	95.8	17.5	16.8
M_{200} (M_\odot) ^b	1.3e15	2.4e14	7.5e14
r_{200} (deg) ^b	1.3	4.1	6.2
\mathcal{J}_{NFW} ^c	5.9e-5	4.1e-4	1.2e-3
Enhancement due to subhalos within r_{200} ^d	1.3e3	6.5e2	1.0e3

^aAngular diameter distance, from the NASA extragalactic database for Coma and Fornax, and from Tully & Shaya (1984) for Virgo.

^bCluster halo mass defined as the mass within the radius, r_{200} , within which the average density equals 200 times the critical density of the universe. Values for Coma and Fornax are taken from Pinzke et al. (2011), while the value for Virgo is taken from Tully & Shaya (1984).

^cIntegrated coefficient, $\mathcal{J}_{int} = \int_{\Delta\Omega} J d\Omega$, over the solid angle spanned by the cluster virial radius, assuming a smooth NFW density profile.

^dEnhancement to the total annihilation luminosity within the virial radius due to substructures, extrapolated to a subhalo mass limit of $10^{-6}M_\odot$. Note this factor scales with the minimum subhalo mass as $M_{cut}^{-0.226}$ (Springel et al. 2008).

The factor $\frac{1}{2}$ comes from the constraint that the normalization parameter be non-negative. The significance of a detection can thus be quoted as $\sqrt{TS}\sigma$ (one-sided Gaussian confidence). Upper limits on the extra normalization parameter N are obtained by searching for a null hypothesis L'_0 where N in the full model is constrained to be equal to the upper limit, N_{UL} , so that $\ln(L'_0/L) = -1.35$, corresponding to the 95% confidence interval.

1.3 Model

For the analysis we constructed a model to fit the data including all known foreground and background emission, as well as DM and CR components, as appropriate. We include all the point sources from 2FGL within a radius of 15 degrees from the cluster centre in the model, plus the most recent galactic (GAL) and extragalactic (EG) diffuse emission given by the template files `gal_2yearp7v6.v0.fits` and `iso_p7v6clean.txt`. Additionally, we have searched the 45-month data for new point sources; we detect several of them within the cluster region (see Appendix A for more detail) and these are also included in our model. The normalization of the GAL and EG diffuse components are allowed to vary during the fitting. Within the cluster virial radius there are two 2FGL point sources and one newly detected point source in Fornax, six 2FGL, including the central AGN (M87; Abdo et al. 2009), plus four newly detected ones in Virgo. We allow the normalization and power-law spectral index of these thirteen point sources to vary freely. In addition, the parameters of all sources with variability index greater than 50 located within 10 degrees of the cluster centres are allowed to vary. Parameters for the other point sources are fixed as in the 2FGL catalog. From now on we refer to the model with GAL, EG and the known point sources as the “base model”.

A DM annihilation surface brightness template (given

by the dimensionless factor J , see Eqn. 4 in Sec. 2.1) is generated for each cluster out to a 15 degree radius by summing up both the contribution from a smooth NFW profile and the contribution from subhalos. This J -map is used to fit for extended cluster annihilation emission. For the point source model, the integrated factor \mathcal{J}_{NFW} (see Eqn. 5) is used to derive an annihilation cross-section from the fitted total flux. Similarly, a CR photon template is generated for each cluster out to three times the cluster virial radius, where the surface brightness has dropped to below 10^{-5} of the central value and beyond which the model is not reliable. Images for various model components are shown in Fig. 1 taking Virgo as an example. We discuss these templates in more details in Sec. 2.

In the traditional Fermi analysis, the EG template is treated as a smooth component where all emission below the nominal point source detection limit is assumed to come from a smoothly distributed diffuse component. In this work, we also consider a more realistic one where a fraction is assumed to be contributed by fainter point sources with a number-flux relation which extrapolates smoothly from that measured for brighter sources. In this case the photon counts within a given pixel are no longer Poisson-distributed since the photons arrive in packets. In principle, one can use the full distribution of photon counts from a population of randomly placed point sources to calculate the likelihoods L and L_0 , but Eqns. 1 and 2, and the corresponding discussion, are not affected. However, since the full distribution of photon counts in this case (Han et.al., in prep.) is complicated and difficult to implement in the likelihood analysis, instead of recalculating L and L_0 , in this work we use Monte-Carlo simulations to re-evaluate the distribution of TS for the more realistic background model and provide corrections to the results of the standard analysis where needed.

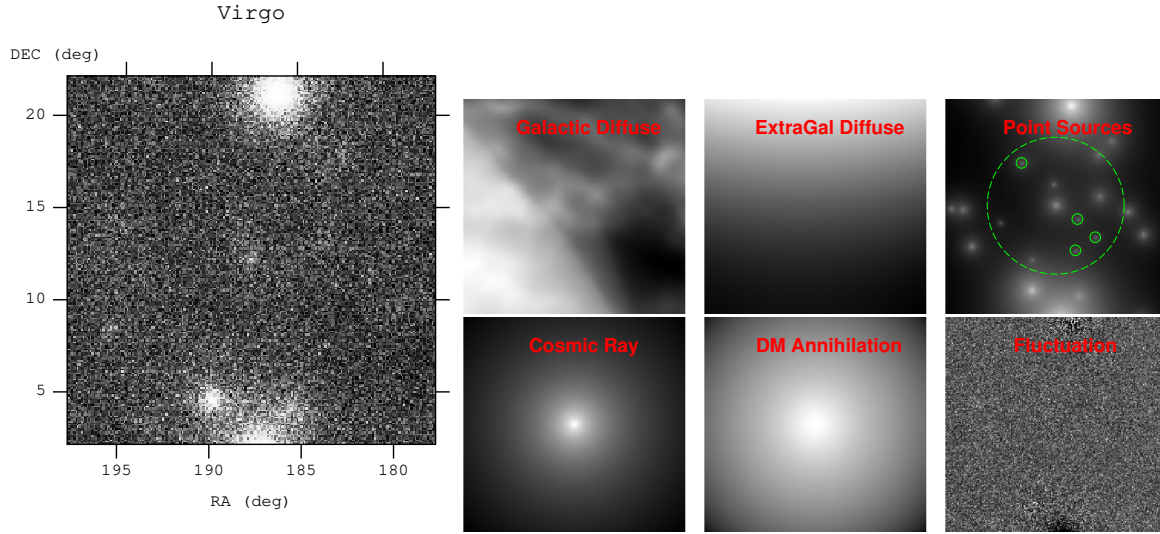


Figure 1. Decomposition of the Fermi-LAT image in the region of the Virgo cluster into model components. The observed photon count image from 100 MeV to 100 GeV is shown on the left. The right panels show the integrated image over the same energy range for the various model components: galactic diffuse emission, extragalactic diffuse emission, detected point sources, cosmic-ray photons and DM annihilation emission, as labeled. The green dashed circle in the “Point Sources” panel marks the virial radius of the cluster. The small circles mark the newly detected point sources which are not present in the 2FGL. The “Fluctuation” panel shows the residual image for our best-fit DM model. The images have been enhanced individually in colour space for contrast. Note the apparent structure in the extragalactic component which is due to different exposure times at different positions.

2 MODELING GAMMA-RAY EMISSION IN CLUSTERS

We model the observed gamma-ray emission in clusters with several components as shown in Fig. 1: the galactic foreground (GAL), the extragalactic background (EG), emission from known point sources, DM annihilation and CR-induced emission. The GAL and EG diffuse emission are given by the most recent templates, `gal_2yearp7v6.v0.fits` and `iso_p7v6clean.txt`, which can be obtained from the Fermi-LAT data server, while the point sources include those from the LAT 2-year point source catalogue, 2FGL (Nolan et al. 2012), as well as several, newly detected by us, in the 45-month data. In addition, an improved EG model which includes a population of un-detected sources is also analyzed. We now describe in detail our models for DM annihilation and CR emission.

2.1 Dark matter annihilation emission

The gamma-ray intensity along the line-of-sight due to DM annihilation is given by:

$$I = \frac{1}{8\pi} \sum_f \frac{dN_f}{dE} \langle \sigma_f v \rangle \int_{l.o.s.} \left(\frac{\rho_\chi}{M_\chi} \right)^2 (l) dl, \quad (3)$$

where M_χ is the DM particle mass; ρ_χ the density of DM; $\frac{dN_f}{dE}$ the particle model dependent term giving the differential number of photons produced from each annihilation event as a function of energy, E , in a particular annihilation channel, f ; and $\langle \sigma_f v \rangle$ is the velocity-averaged cross-section (or annihilation rate) for that channel, which is predicted to be constant in the low velocity limit appropriate to present-day cold DM particles (see e.g., Jungman et al.

(1996)). The line-of-sight integration of the density squared is often expressed in terms of a dimensionless factor,

$$J = \frac{1}{8.5\text{kpc}} \left(\frac{1}{0.3\text{GeV}/\text{cm}^3} \right)^2 \int_{l.o.s.} \rho_\chi^2(l) dl. \quad (4)$$

If the source size is much smaller than the instrumental beam size, a point source approximation is applicable. In this case, the integration of J over a large enough solid angle, $\Delta\Omega$, is used to determine the total flux for the point source, $\mathcal{J}_{int} = \int_{\Delta\Omega} J d\Omega$.

The cluster annihilation emission is modeled with the extended profile suggested by Gao et al. (2012). However, for part of the analysis and for comparison purposes, we will also use the point source approximation which, although inappropriate, has been employed in all previous analysis of Fermi-LAT data from clusters. We shall refer to models that assume these two profiles respectively as EXT and PT. If the cluster follows a smooth NFW profile, then its integrated J factor which determines the total annihilation flux can be found as

$$\mathcal{J}_{NFW} = \frac{4\pi}{3} \rho_s^2 r_s^3 \frac{1}{D_A^2} \times \frac{1}{8.5\text{kpc}} \left(\frac{1}{0.3\text{GeV}/\text{cm}^3} \right)^2. \quad (5)$$

Here D_A is the angular diameter distance to the cluster and ρ_s and r_s are the characteristic density and radius of the NFW profile. They are related to halo concentration, c , and virial radius through the relations, $\rho_s = \frac{200}{3} \frac{c^3 \rho_c}{\ln(1+c) - c/(1+c)}$ and $r_s = r_{200}/c$, with ρ_c the critical density of the universe, r_{200} the cluster virial radius within which the average density is $200\rho_c$ and the concentration parameter, c , is given by the following mass-concentration relation:

$$c = 5.74 \left(\frac{M_{200}}{2 \times 10^{12} h^{-1} M_\odot} \right)^{-0.097} \quad (6)$$

(Duffy et al. 2008). Here, M_{200} is the mass enclosed within r_{200} . Extrapolating to a cutoff mass of $10^{-6}M_{\odot}$, the existence of subhalos will increase this flux by a factor

$$b(M_{200}) = \mathcal{J}_{sub}/\mathcal{J}_{NFW} = 1.6 \times 10^{-3}(M_{200}/M_{\odot})^{0.39} \quad (7)$$

Gao et al. (2012). Using the results of the simulations by these authors, the surface brightness profile of subhalo emission can be fitted within r_{200} by the following formula:

$$J_{sub}(r) = \frac{16b(M_{200})\mathcal{J}_{NFW}}{\pi \ln(17)} \frac{D_A^2}{r_{200}^2 + 16r^2} \quad (r \leq r_{200}). \quad (8)$$

Below we fit the subhalo emission surface brightness beyond the virial radius and extrapolate to several times the virial radius using an exponential decay,

$$J_{sub}(r) = J_{sub}(r_{200})e^{-2.377(r/r_{200}-1)} \quad (r \geq r_{200}). \quad (9)$$

The total annihilation profile is the sum of the contributions from a smooth NFW profile and the subhalo emission. This is completely dominated by subhalo emission except in the very centre of the cluster. We show the total annihilation profile and its decomposition into main halo and subhalo contributions in the left panel of Fig. 3, taking Virgo as an example. This profile is further inflated after convolution with the LAT point spread function.

We consider three representative annihilation channels, namely into $b\bar{b}$, $\mu^+\mu^-$ and $\tau^+\tau^-$ final states. The annihilation spectrum is calculated using the DarkSUSY package (Gondolo & Silk 1999),¹¹ which tabulates simulation results from PYTHIA.¹² We also include the contribution from inverse Compton (IC) scattered photons by energetic electron-positron pairs produced during the annihilation process, following the procedure described in Pinzke et al. (2011). In general, three external energy sources are involved in the dissipation and scattering of the injected electrons from annihilation: the Cosmic Microwave Background (CMB), infrared to UV light from stars and dust, and the interstellar magnetic field. However, as shown by Pinzke et al. (2011), the latter two components are expected to be important only in the inner region of clusters ($< 0.03r_{200}$), corresponding to less than 0.2 degrees for our three clusters. Including them would introduce a position-dependent component to the annihilation spectrum, so for simplicity we only consider the contribution of CMB photons in the IC calculation. For the $b\bar{b}$ channel, IC photons only contribute significantly to the low energy spectrum for relatively high neutralino mass, while for the leptonic channels, which have plenty of energetic electrons, the IC emission can completely dominate the annihilation emission over the full energy range of interest for the highest neutralino masses considered.

We note that the electroweak corrections recently proposed by Ciafaloni et al. (2011) (see also Cirelli et al. (2011)) can bring visible differences to the leptonic channel spectra at high WIMP masses before IC scattering. However, since IC photons dominate at the high mass end and the electroweak correction only significantly changes the positron yields at low energy, thus having little effect on the IC spectrum, the electroweak correction to the total spectrum is still negligible. The total photon yields are shown in Fig. 2.

The almost flat spectrum with a cutoff around the energy corresponding to the WIMP mass comes from prompt annihilation emission including continuum secondary photons and final state radiation from charged final state particles. The low energy rise originates from IC scattered CMB photons.

2.2 Cosmic-ray induced gamma-ray emission within clusters

The cosmic ray induced gamma-ray emission is calculated following a semi-analytic prescription, derived from high resolution numerical simulations of galaxy clusters, that models cosmic ray physics self consistently (Pinzke & Pfrommer 2010). The gamma-ray photon production rate (or source function) from pion decay is found to be separable into a spatial and a spectral part:

$$q_{CR}(r, E) \equiv \frac{dN_{\gamma}}{dt dV dE} = A(r)s(E), \quad (10)$$

where the spatial part, $A(r)$, is proportional to the square of the gas density profile multiplied by a slowly varying radial function parametrized by cluster mass. The spectral part, $s(E)$, is almost independent of cluster mass and has a power-law form, $dN_{\gamma}/d\ln(E_{\gamma}) \propto E_{\gamma}^{-1.3}$, for the energy range 1 ~ 100 GeV but flattens at low energies, as shown in Fig. 2. We summarize the detailed form of $A(r)$ and $s(E)$ plus the gas density profile for the three clusters derived from X-ray observations in the Appendix.

The differential gamma-ray flux from this source function, $I_{CR}(r, E)$, is simply the integral of $q_{CR}(r, E)$ along the line-of-sight. This prescription is derived from the average emission profile for a sample of simulated clusters for a realistic choice of parameter values (e.g., for the maximum shock acceleration efficiency, $\zeta_{p,max}$). In addition to the uncertainties in the model parameters there is also uncertainty in the observationally derived halo mass and gas density profile. In this work, we simply assume that the shape of $q_{CR}(r, E)$ is given by the model described above and account for the uncertainty in the model parameters, as well as sample variance with an additional normalization parameter, α_{CR} , so that,

$$I_{CR}(r, E) = \alpha_{CR} \int_{l.o.s} \frac{q_{CR}(r, E)}{4\pi} dl. \quad (11)$$

We take $\alpha_{CR} = 1$ as our fiducial CR model and also consider the case when α_{CR} is fitted from the actual gamma-ray data as an optimal model. In the right panel of Fig. 3 we compare the CR profile for the fiducial model to the expected DM annihilation profile within our three clusters, assuming a fiducial DM particle model with particle mass, $M \approx 100\text{GeV}$, annihilating through the $b\bar{b}$ channel with cross-section, $\langle \sigma v \rangle = 3 \times 10^{-26} \text{cm}^3 \text{s}^{-1}$. In general the CR emission is more centrally concentrated than the annihilation profile since the CR trace the gas profile. It can be readily seen that Fornax has a particularly low CR level while Coma is CR dominated. Coma has steeper profiles due to its larger distance and hence smaller angular size.

¹¹ <http://www.darksusy.org>.

¹² <http://home.thep.lu.se/~torbjorn/Pythia.html>

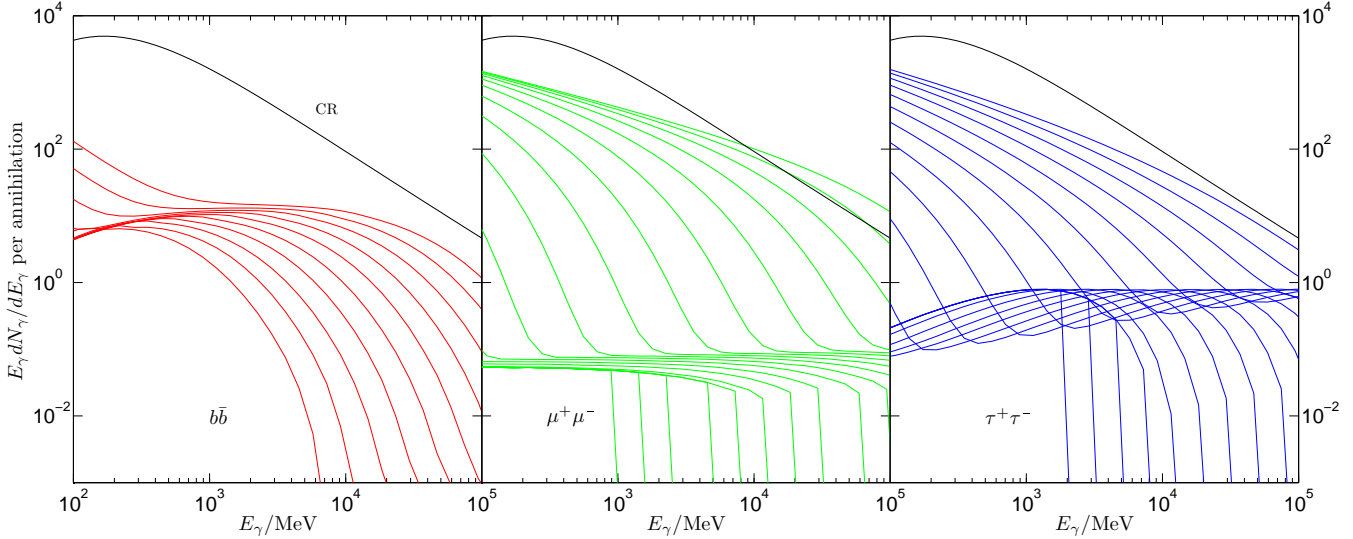


Figure 2. Photon yields for $b\bar{b}$ (left), $\mu^+\mu^-$ (middle) and $\tau^+\tau^-$ (right) channels. Plotted are the total photon yields including continuum secondary photons, final state radiation from charged final state particles, as well as inverse Compton scattering of CMB photons by electron/positron pairs, for the mass range 10 – 1000 GeV for the $b\bar{b}$ channel, 1GeV – 10TeV for the $\mu^+\mu^-$ channel and 2GeV – 10TeV for the $\tau^+\tau^-$ channel. The masses are sampled uniformly in a log scale. Note that each spectrum cuts off at an energy corresponding to the particle mass. For comparison, the black line in each panel shows the photon spectrum from cosmic ray induced photons with arbitrary normalization.

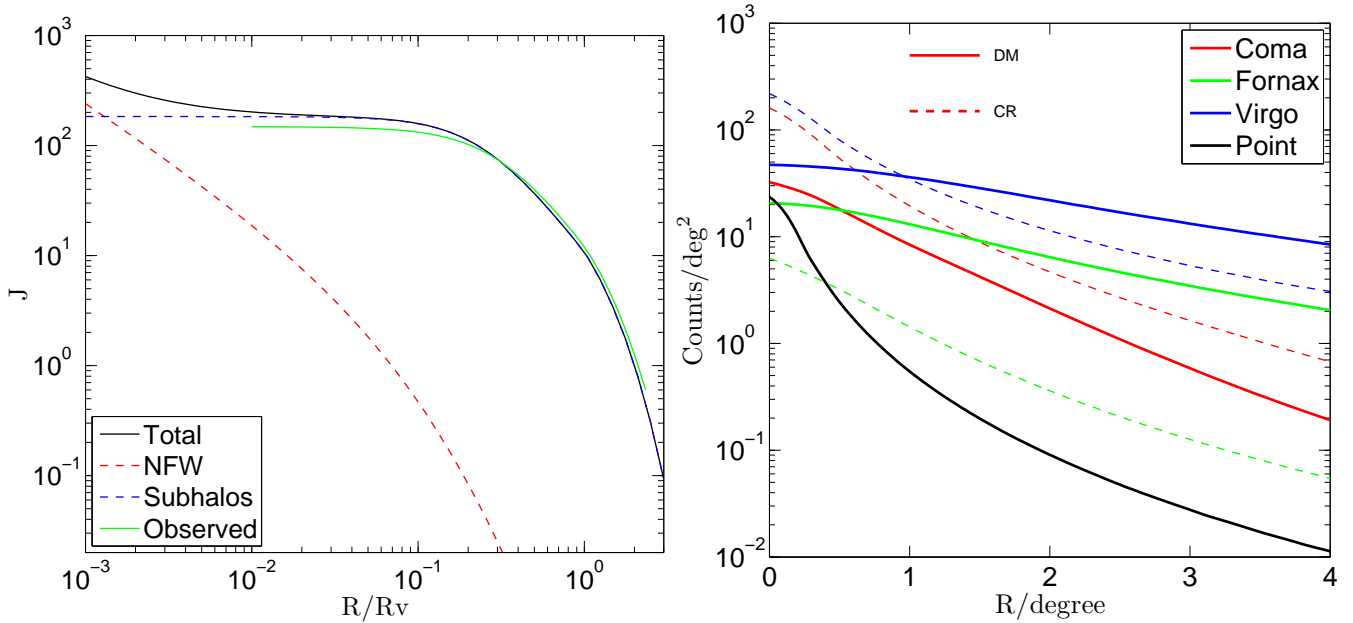


Figure 3. Cluster photon profiles. Left: theoretical and PSF-convolved J profile for Virgo. The total annihilation profile is shown as a black solid line and is decomposed into the smooth main halo part (red dashed line) and the subhalo part (blue dashed line). The green solid line shows the annihilation profile after PSF convolution, plotted down to an inner radius comparable to the pixel size of 0.1 deg. Right: PSF-convolved photon profiles for annihilation (solid) and cosmic rays (dashed) for three clusters (indicated by different colours). Solid lines show the expected photon count profile for the extended DM annihilation model. Dashed lines show the expected cosmic-ray induced photon counts for the fiducial CR model. For comparison, we also plot the PSF-convolved profile for a central point source (black solid line) with arbitrary normalization. In both panels, a dark matter model with particle mass, $M \approx 100\text{GeV}$, and annihilation cross-section, $\langle \sigma v \rangle = 3 \times 10^{-26} \text{cm}^3 \text{s}^{-1}$, through the $b\bar{b}$ channel is assumed. The PSF convolutions are done with the `gtmodel` tool in the Fermi Science Tools software package.

3 RESULTS

3.1 Constraints on CR emission

With all the model components defined above, we first proceed with ML fitting for a model with no DM annihilation but with cosmic rays, the “CR-only” model hereafter. Note that the GAL and EG backgrounds, as well as the nearby point sources, are always included in the analysis, as described in section 1.2. The results for the CR-only model fits are listed in Table 2. The fitted CR levels all agree within a factor of three with the theoretical predictions. While Fornax is most consistent with no CR emission due to its intrinsically low CR level, the derived upper limit for Coma already rules out the fiducial value at 95% confidence.

3.2 Constraints on DM annihilation

Given the low significance of the CR detection in the CR-only model, it is not safe simply to adopt the best fit α_{CR} values for further extraction of the DM signal. Instead, we consider the following four families of cosmic ray models in the presence of a DM component:

Fiducial-CR model. The CR level is fixed to the theoretical expectation, $\alpha_{CR} = 1$. Since this value exceeds our derived upper limit for Coma, we exclude Coma from further discussion of this family.

Optimal-CR model. The CR level is taken as the best-fit value listed in Table 2.

Free-CR model. The normalization of the CR level is left as a free parameter in the fit.

No-CR model. No CR emission is considered, only DM.

For each family, both point source (PT) and extended (EXT) profiles are considered for the DM component (the former merely for comparison with earlier work). Note that when calculating the TS for DM, the null hypothesis refers to the full model excluding only the DM component, or equivalently, to the base model plus a CR component modelled according to one of our four families of CR models. We show results for the $b\bar{b}$, $\mu^+\mu^-$ and $\tau^+\tau^-$ DM annihilation channels.

For none of the combinations of DM and CR models considered here, do we obtain a detection of DM at high significance in any of the three clusters. The highest significance is obtained for Virgo for the $b\bar{b}$ channel in a DM model that has a particle mass of 30 GeV and the EXT profile, in the absence of CR. In this case, we find $TS = 11.6$, corresponding to 3.4σ . This reduces to 2.6σ in the Free-CR model and to less than 1σ in the Fiducial-CR model.

The value of $TS = 11.6$ for the no-CR model for Virgo can be compared with the value of $TS = 24$ reported in an earlier version of this paper (arXiv:1201.1003v.1) from a similar analysis of the 2-year Virgo data (see Fig. 4). The decrease in significance is entirely due to the subtraction of the new point sources which we have detected in the Virgo region and which were not catalogued in the 2FGL. These previously undetected sources happen to lie within the virial radius of Virgo and can mimic the extended emission expected from DM annihilation. In fact, fits assuming an EXT profile but a power-law, rather than a DM annihilation spectrum, result in a similarly high significance detection, $TS = 21$,

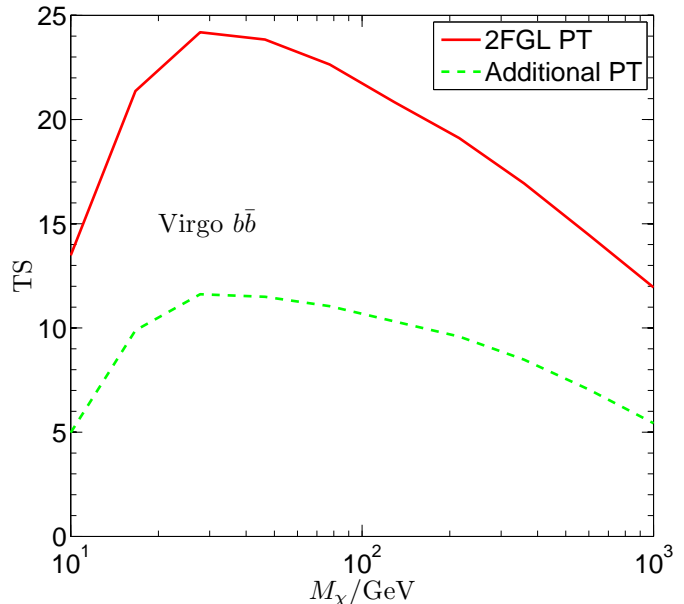


Figure 4. The significance of a DM component in Virgo, with $b\bar{b}$ final states, in the absence of CR. The solid line shows the TS when only 2FGL sources are included in the model, while the dashed line shows the case when the four new point sources that we have detected are also included.

and a best-fit spectral index $\Gamma = -1.9$. This is the typical spectral index of Fermi point sources (including the newly detected ones). The preference for a 30 GeV DM particle mass in the DM fits reflects a preference for a $\Gamma = -1.9$ spectrum around 1 GeV, the energy scale from which most of the significance arises.

In fact, the significance of the Virgo detection is further reduced when we take account in the analysis of a possible undetected point source population, as we shall do in Appendix B. Thus, in what follows we use our analysis exclusively to set upper limits on the flux and annihilation cross-section.

3.2.1 The $b\bar{b}$ channel

In Fig. 5 we show the 95% confidence upper limits on the DM annihilation flux and compare them to the CR levels. For each cluster, the coloured stripes are defined by the minimum and maximum upper limits corresponding to the four families of CR models. The optimal CR levels in the three clusters are all comparable to the fitted DM flux, and the DM flux upper limits for the four different CR models vary only within a factor of two, with the No-CR and Fiducial-CR¹³ cases predicting the highest and lowest upper limits. The left and right panels show the results for the EXT and PT models respectively; the PT models always have lower flux upper limits than the extended models.

The flux upper limits are translated into cross-section upper limits in Fig. 6, using Eqn. 3. These are also shown as coloured regions reflecting the variation in the different

¹³ In Coma, where the Fiducial-CR model is ruled out, the Optimal-CR model yields the lowest upper limit.

Table 2. Fits to the CR-only Model

	$\alpha_{CR,fit}^a$	$\alpha_{CR,UL}^b$	$F_{CR,UL}^c(\text{ph} \cdot \text{cm}^{-2} \text{s}^{-1})$	TS	$TS_{corrected}^d$	$\alpha_{CR,UL,corrected}^e$
Coma	0.3 ± 0.1	0.5	2.4e-09	5.2	2.6	0.6
Fornax	0.9 ± 2	4.8	1.8e-09	0.2	0.1	6.4
Virgo	0.6 ± 0.3	1.2	2.1e-08	8.4	2.8	1.6

^aBest fit normalization ($\alpha_{CR,fit} = 1$ is the theoretical prediction)

^b95% upper limit (UL) on the normalization

^c95% upper limit on the CR induced gamma-ray flux from 100 MeV to 100 GeV

^dTS after allowing for undetected point sources; see Section 3.3 for details

^eUpper limit on the normalization factor after allowing for undetected point sources; see Section 3.3 for details

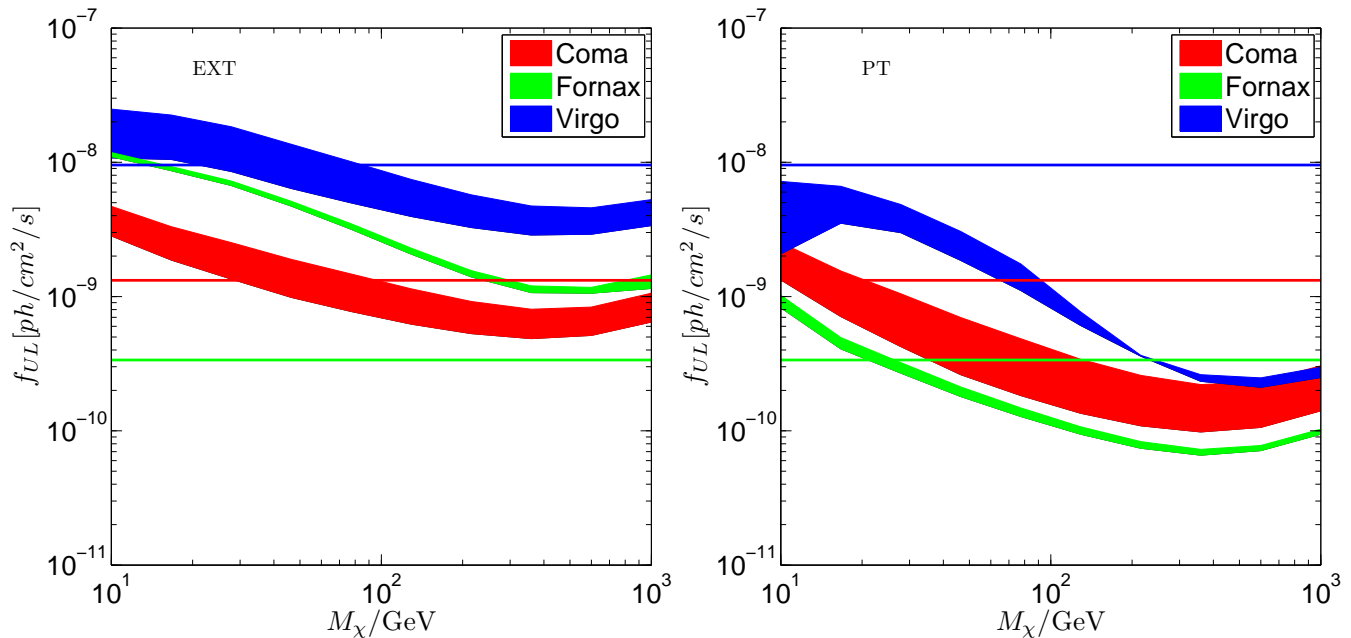


Figure 5. DM annihilation flux upper limits for the $b\bar{b}$ channel. The stripes are defined by the minimum and maximum upper limits given by the four CR model families, with different colours corresponding to different clusters, as indicated in the legend. Left and right panels are the results for the EXT and PT profiles respectively. For each cluster, a solid line of the corresponding colour shows the optimal CR flux.

treatments of CR. Although the predicted flux upper limits decrease slowly with DM particle mass and remain within the same order of magnitude for the mass range considered, the resulting cross-section upper limits increase by a factor of 100 from low to high particle mass. This is because low mass particles correspond to higher DM number densities (the ρ_χ^2/M_χ^2 factor in Eqn. 3) for a given mass density, so to obtain the same flux level, the required cross-section must be smaller for low mass particles. With an enhancement of order 10^3 due to subhalos, a much lower cross-section is needed (by a factor of at least 100) for extended annihilation models to achieve a slightly higher flux upper limit than point source models.

Our cross-section limits drop below the fiducial thermal cross-section of $3 \times 10^{-26} \text{cm}^3 \text{s}^{-1}$ for $M_\chi \lesssim 100 \text{GeV}$. Of the three clusters, Virgo has the highest flux upper limits but it still places the tightest constraints on the annihilation

cross-section. Our limits are much lower than those in the 11-month Fermi-LAT analysis by Ackermann et al. (2010), where the tightest constraint came from Fornax for a much lower assumed subhalo contribution of ~ 10 . Our limits are also tighter than that from a joint analysis of the dwarf satellites of the Milky Way by Geringer-Sameth & Koushiappas (2011).¹⁴ Note that the difference between our results and that of Ackermann et al. (2010) comes mostly from different assumptions about the effect of subhalos, and only secondarily from the larger amount of data we have analysed. Also, note that in the analysis of Geringer-Sameth & Koushiappas

¹⁴ If systematic uncertainties in the halo mass parameters assumed by Geringer-Sameth & Koushiappas (2011) are considered, the lower bounds of their derived limits become comparable to our limits.

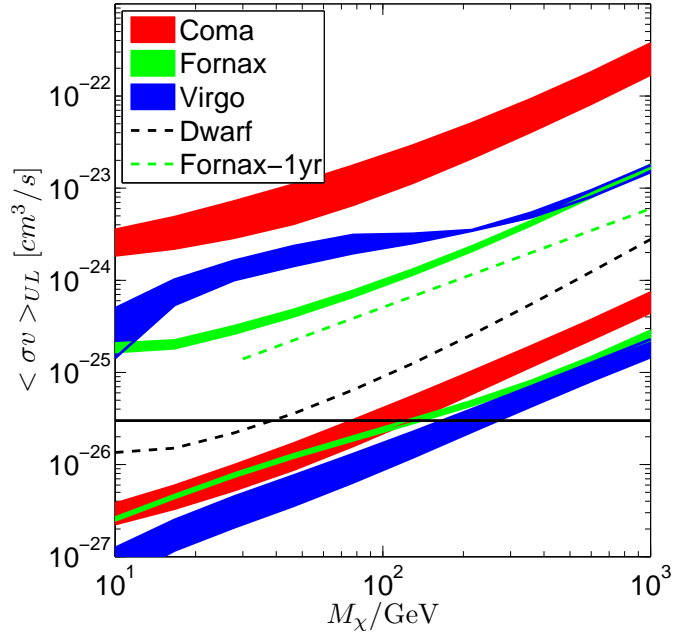


Figure 6. Upper limits for the DM annihilation cross-section in the $b\bar{b}$ channel. The different colours represent the three clusters, with the stripes spanning the range between the minimum and maximum upper limits given by the four different ways of treating the CR component. The three highest stripes show the PT model constraints and the three lowest the EXT model constraints. We also plot with dashed lines constraints^b from a joint analysis of the Milky Way dwarf galaxies (Geringer-Sameth & Koushiappas 2011, black dashed line) and previous constraints from the 11-month Fermi-LAT data for Fornax (Ackermann et al. 2010, green dashed line) assuming these authors’ optimistic value for the total enhancement due to subhalos, which gives the tightest constraint. The black solid line indicates the canonical thermal cross-section of $3 \times 10^{-26} \text{cm}^3 \text{s}^{-1}$.

^a The “Fermi-1yr” constraint is only reproduced schematically, by reading out several data points from the original plot in the reference.

^b The “Fermi-1yr” constraint is only reproduced schematically, by reading out several data points from the original plot in the reference.

(2011), no boost from subhalos within the halo of dwarf galaxies was assumed.

3.2.2 The $\mu^+\mu^-$ channel

As have been seen in section 3.2.1, the EXT model places tighter constraints on the cross-section than the PT model, and is the fiducial model expected from recent simulations. Therefore from now on we will only show results for the EXT model. The flux and cross-section upper limits for DM annihilating through the $\mu^+\mu^-$ channel are plotted in Figs 7 and 8. The predicted flux upper limits for Coma and Virgo are still comparable to the CR level, with Fornax having much lower CR emission. The inferred cross-section falls below the canonical value for DM particle masses less than 10 GeV. Note the discontinuity in the upper limits around 100 GeV which reflect the transition from the prompt annihilation dominated regime to the IC emission dominated regime in the photon spectrum.

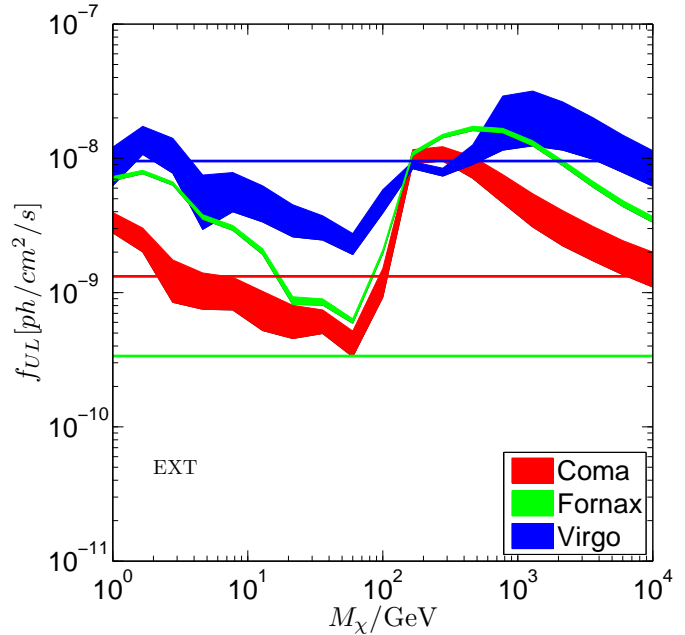


Figure 7. DM annihilation flux upper limits in the $\mu^+\mu^-$ channel for the EXT model. Line styles are as in Fig. 5.

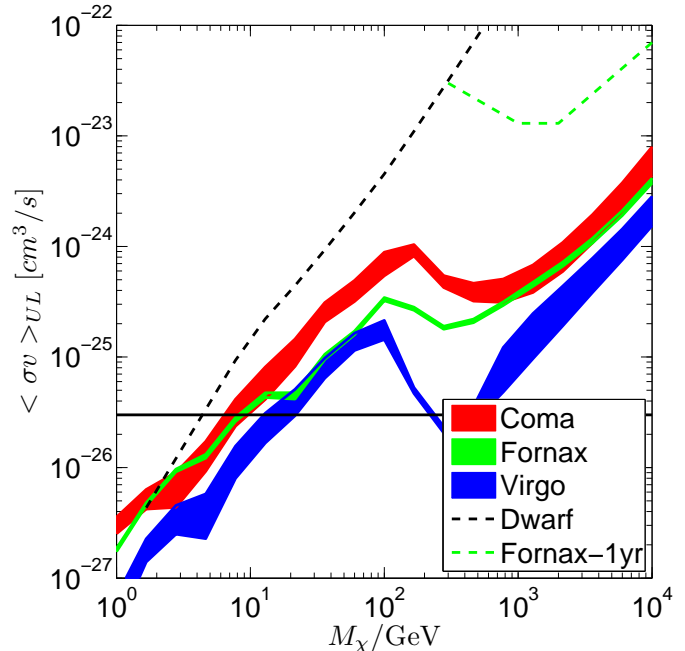


Figure 8. Upper limits for the DM annihilation cross-section in the $\mu^+\mu^-$ channel. Line styles are as in Fig. 6, but only the EXT results are shown. The green dashed line is the 11-month Fermi result (Ackermann et al. 2010) for Fornax while the black dashed line is the dwarf galaxy constraint (Geringer-Sameth & Koushiappas 2011), both for the $\mu^+\mu^-$ channel.

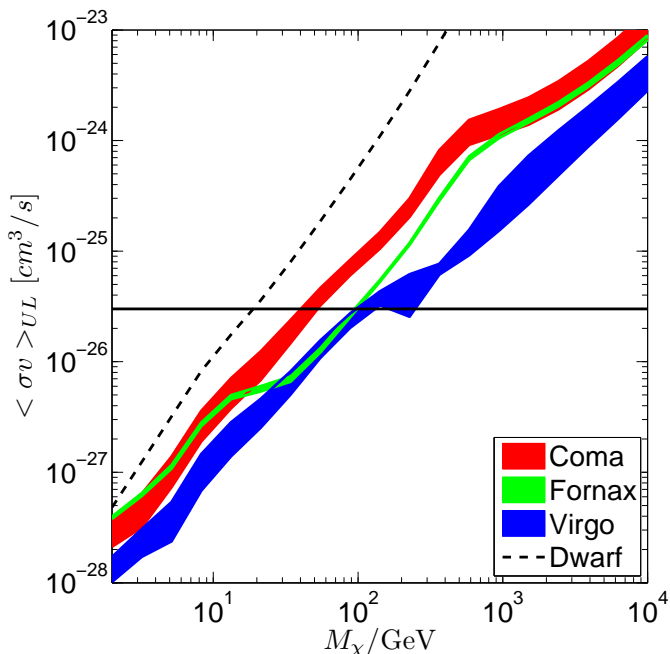


Figure 9. Upper limits for the DM annihilation cross-section in the $\tau^+\tau^-$ channel. Line styles are as in Fig. 6, but only the EXT results are shown. The black dashed line is the dwarf galaxy constraint. (Geringer-Sameth & Koushiappas 2011)

3.2.3 The $\tau^+\tau^-$ channel

In Fig. 9 we show the cross-section upper limits for the $\tau^+\tau^-$ channel. This is the primary component of the leptonic model used by Hooper & Linden (2011b) to fit the excess gamma-ray emission in the Galactic centre region.

3.3 Allowing for an undetected point source population

Although we have detected five new point sources in the 45-month data in the region of our three clusters, it is still necessary to account for population of still undetected point sources. When no unknown point sources are present, the probability of measuring a certain value of TS when the null hypothesis is true is given by the probability that Poisson fluctuations in the photon counts for the null model exceed some value. When a population of undetected point sources is present, the Poisson fluctuations become correlated and it is easier for the same amplitude of fluctuations to result in a given value of TS . In this case, the distribution of TS no longer follows the χ^2 distribution, as predicted by Wilk’s theorem, because the data no longer follow a pure Poisson distribution from which the likelihood function is constructed.

Allowing for the presence of undetected point sources in the data will lead to weaker upper limits. We obtain these by performing Monte-Carlo simulations to re-calibrate the significance corresponding to a given value of TS . In the simulations we include the GAL and 2FGL sources, but we split the EG component into two parts: a population of undetected point sources and a residual smooth EG component, such that the sum of the two is consistent with the standard

EG component. We consider a benchmark model for the undetected point source population which is close to the model derived by Abdo et al. (2010) and which contributes 14% of the EG background. Details of the simulations may be found in Appendix B. A standard likelihood analysis is then performed on the simulated data in order to derive appropriate values of TS for an assumed DM or CR component.

With the introduction of the undetected point source population, the distribution function for TS is found to be roughly described by $\chi^2(TS/b)/2$. That is, the significance of a given value of TS is approximately reduced by a factor of b compared to the significance of the same value of TS in the absence of the undetected point source population. For a DM component, we find $b \sim 2$ for Coma and $b \sim 3$ for Virgo and Fornax. The b factor is not sensitive to the adopted DM spectrum. For the CR models, we find $b \sim 2$ for Coma and Fornax, and $b \sim 3$ for Virgo.

In order to obtain new limits from the corrected TS, let us first consider the likelihood function that has been maximized over all the nuisance parameters. Expanding around the maximum likelihood value of the parameter N to leading order, we have

$$\ln L(N_0) = \ln L(N) - \frac{1}{2}H(N_0 - N)^2, \quad (12)$$

where $H = -\frac{d^2 \ln L}{dN^2} = \frac{1}{\sigma_N^2}$ is the Hessian matrix. The 95% upper limit is calculated from $\ln L(UL) - \ln L(N) = -1.35$, so that

$$UL = N + 1.64\sigma_N. \quad (13)$$

Note that $\frac{N}{\sigma_N} = \sqrt{TS}$. Similar equations hold for the improved background model, with UL , σ_N and TS replaced by UL' , σ'_N and TS' respectively, assuming that there is no bias in the best-fit parameters. The 95% upper limit is then corrected for the undetected point source fluctuations according to

$$UL' = \frac{\sqrt{TS} + 1.64\sqrt{TS'/TS}}{\sqrt{TS} + 1.64} UL, \quad (14)$$

where UL and TS are the upper limit and likelihood ratio from the standard analysis, while UL' and TS' are the corrected upper limit and likelihood ratio. For $b = 3$, the increase in the upper limit is at most 70%.

In Fig. 10, we show the corrected dark matter annihilation cross-section upper limits adopting $b = 2$ for Coma and $b = 3$ for Virgo and Fornax. The corrected TS and upper limits for CR models are listed in the last two columns of Table 2.

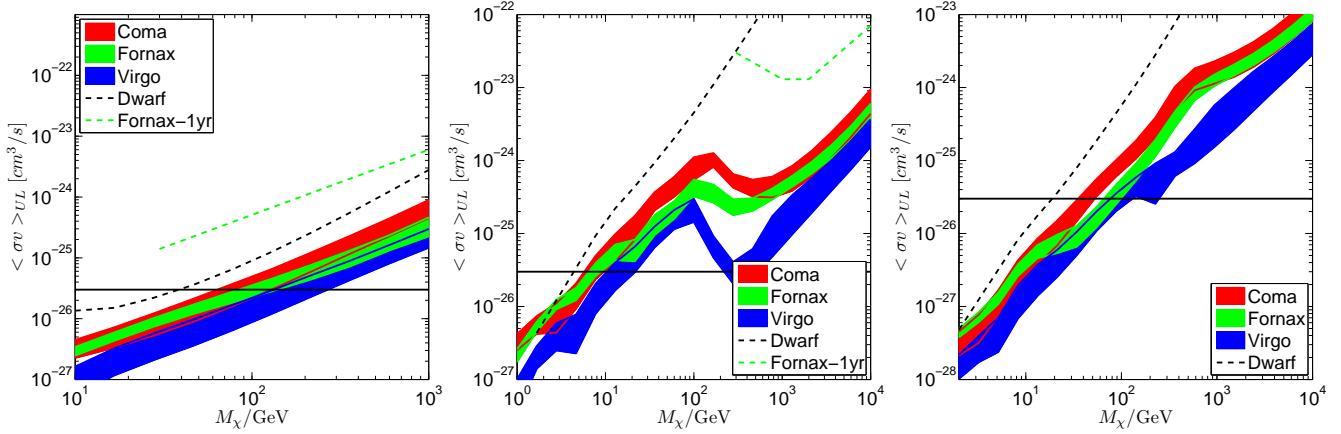


Figure 10. Upper limits for the DM annihilation cross-section in the $b\bar{b}$ (left), $\mu^+\mu^-$ (middle), and $\tau^+\tau^-$ (right) channels, after including the effect of undetected point sources. Line styles are as in Fig. 6, but only the EXT results are shown. Note that the lower bounds of each band are still determined by the results without including undetected point sources in the analysis.

4 DISCUSSION AND CONCLUSIONS

We have performed maximum likelihood fits to the 3-year Fermi-LAT data for three galaxy clusters: Coma, Fornax and Virgo. We fit models which, in addition to point sources and galactic and extragalactic backgrounds, include emission due to dark matter (DM) annihilation and cosmic rays (CR). For the former, we assume both a point source and the theoretically predicted extended distribution of gamma rays in three generic annihilation channels, the $b\bar{b}$, $\mu^+\mu^-$ and $\tau^+\tau^-$ channels. When searching for a dark matter signal, we experiment with different treatments of the CR component. In the traditional Fermi analysis, the extragalactic background (EG) is assumed to be a smooth component. In this work we have also investigated a more realistic EG model where a fraction of the EG emission comes from a population of undetected point sources.

Performing a standard likelihood analysis we obtain the following results:

(i) In all three clusters and for the four different treatments of CR we have implemented, no significant detection of DM emission is obtained. We set upper limits on the flux and cross-section of DM annihilation in the three clusters we have investigated. Uncertainties in the CR component have only a mild effect on the upper limits: for the different CR models, the DM upper limit constraints agree to within a factor of two.

Models in which the DM annihilation emission has the extended profile predicted by cosmological simulations (Gao et al. 2012) have higher flux upper limits than models in which this emission is assumed to be a point source. Due to the large luminosity enhancement, of order of 1000, by emission from subhalos, the upper limits on the annihilation cross-section for extended models are at least 100 times lower than those for point source models. Our cross-section constraints are much tighter than those from an analysis of clusters using the 11-month data (Ackermann et al. 2010), mostly because we take into account the effect of subhalos. Our constraints are also tighter than those from a joint analysis of Milky Way dwarf galaxies

(Geringer-Sameth & Koushiappas 2011; Ackermann et al. 2011).

Our new limits exclude the thermal cross-section for $M_\chi \lesssim 100$ GeV for $b\bar{b}$ and $\tau^+\tau^-$ final states, and for $M_\chi \lesssim 10$ GeV for $\mu^+\mu^-$ final states. We note that the annihilation cross-section in dark matter halos need not be the standard thermal cross-section of supersymmetric models. In cases where the cross-section is velocity dependent, for example, through p-wave contributions at freeze-out (see e.g., Jungman et al. (1996)), one can easily have a different average cross-section. We emphasize that there is still a large uncertainty our adopted annihilation profile, which depends on a significant extrapolation of the resolved subhalo population by more than 10 orders of magnitude in mass. Taking this into account, the thermal cross-section, however, could still be reconciled with the data by assuming a larger cutoff mass in the WIMP power spectrum, thus reducing the contribution from subhalos and hence the J factor. Since the total enhancement from subhalo emission scales as $b \propto M_{cut}^{-0.226}$ (Springel et al. 2008), a cut-off mass of $10^{-4}M_\odot$, rather than our assumed $10^{-6}M_\odot$, would be sufficient to increase the cross-section limits by a factor of 3.

(ii) Assuming no DM annihilation radiation, the gamma ray data for Coma and Virgo already set significant constraints on the CR level. For Virgo, the data are consistent with the predictions of the analytic CR model proposed by Pinzke & Pfrommer (2010) and Pinzke et al. (2011) while, for Coma, the data place an upper limit that is a factor of two below the analytical prediction, indicating either an uncertainty in model parameters such as halo mass, gas density and maximum shock injection efficiency, $\zeta_{p,max}$, or a peculiarity of the CR emission in Coma. If attributed to $\zeta_{p,max}$, the upper limit on the normalization parameter, α_{CR} , translates into an upper limit on $\zeta_{p,max}$ of 0.3, assuming a linear form for $g(\zeta_{p,max})$. This is consistent with the estimates obtained independently by Zimmer et al. (2011) for Coma using Fermi data and by the Aleksić et al. (2012) for the Perseus cluster using MAGIC observations. If interpreted as an error in the halo mass, a reduction in mass by a factor of 1.6 is required to reconcile the model with the upper limits, assuming a simple CR luminosity scaling relation, $L_\gamma \propto M_{200}^{1.46}$

(Pinzke & Pfrommer 2010), or a factor of 4.3 according to Eqn. D1 in the case when the gas density profile is fixed from X-ray observations. For Fornax, the zero-significance of a CR component is consistent with the low level predicted by the model.

(iii) Five new point sources with $TS > 25$ in Virgo and Fornax have been detected in the 45-month data. Ignoring these new point sources results in a $\sim 5\sigma$ detection for a DM component in Virgo, in contrast to a $\sim 3\sigma$ detection when account is taken of these point sources.

In addition to the standard likelihood analysis, we have also investigated a model in which the EG component includes a population of undetected point sources whose number-flux relation extrapolates smoothly that of the detected sources. Using Monte-Carlo simulations, we find that the standard Fermi likelihood analysis could overestimate the TS of extended emission by a factor of 2 – 3, and underestimate the upper limits by up to 70 percent. Adopting this more realistic EG model yields slightly looser upper limits, but does not quantitatively change any of the above conclusions. Still, it should be kept in mind that these corrections are derived from simulations assuming a particular distribution for the point source population. It is too computationally expensive to explore the parameter space of point source populations with Monte-Carlo simulations. A more detailed and more general analytical study of the effect of undetected point sources will be presented elsewhere (Han et. al., in preparation).

In our analysis we have allowed the parameters of 2FGL point sources lying within the cluster virial radius to vary. This accounts for possible corrections to the 2FGL parameters in the presence of a DM or a CR component, while also avoiding the risk of refitting sources lying near the boundary of the data region with less accuracy. The parameters of highly variable sources are also kept free since the 2FGL parameters for these sources would be the average during a 2 year period whereas here we have 45 months of data. However, we also tried keeping all the point sources fixed or allowing the parameters of all the point sources within the data region to vary during the fitting. We find that this freedom in the treatment of the point sources has little impact on the DM model fits.

The cluster annihilation luminosity scales roughly linearly with halo mass, with the shape of the profile being almost independent of halo mass or concentration when expressed in terms of the normalized radius r/R_{200} . We investigate the effect of mass uncertainties in Appendix E. We have also checked that the different energy cuts assumed in our analysis and in that of Huang et al. (2012) have no effect on the derived upper limits. We are able to reproduce the upper limits on the annihilation cross-section of Huang et al. (2012) for the test case of the Fornax cluster with 3-year data, after adopting the same instrument response function and correcting for slightly different assumed subhalo contributions.

The CR model used in this analysis is still subject to improvement. This model is derived from simulations which, unavoidably, make simplifying assumptions. For example, the simulations only consider advective transport of CR by turbulent gas motions but there are other processes such as CR diffusion and streaming which may flatten the CR pro-

files (Enßlin et al. 2011). In particular, if the CR diffusion is momentum dependent this will entangle the spectral and spatial profile of CR and modify the morphology as well as the spectrum of the CR emission, thus invalidating our basic assumption that α_{CR} is the only free parameter. There could also be CR injected from AGN which are not accounted for in the current model.

Although we have not detected DM annihilation emission in our small cluster sample, the signal-to-noise ratio can potentially be enhanced by stacking many clusters. Such an analysis was recently carried out by Huang et al. (2012), but the signal-to-noise was degraded because of their assumption of an NFW annihilation profile. These authors considered an extended subhalo-dominated annihilation profile but only for individual clusters, not for the stack. Their stacked analysis placed looser constraints on DM annihilation emission than their analysis of individual clusters, presumably because the use of an inappropriate theoretical profile resulted in the different clusters yielding inconsistent results. Thus, it is clearly worth repeating the joint analysis with the “correct” subhalo-dominated profile. It is also tempting to extend the search for DM annihilation using multi-wavelength data, from the radio to very high energy gamma-rays and even in the neutrino channel (Dasgupta & Laha 2012), where different systematics are expected for different bands.

ACKNOWLEDGMENTS

We thank Shaun Cole, Jie Liu, Yu Gao, John Lucey, Anders Pinzke, Christoff Pfrommer, Dan Hooper, Neal Weiner, Douglas Finkbeiner, Gregory Dobbler, Louie Strigari, Christoph Weniger, Savvas Koushiappas, and Fabio Zandanel for helpful discussions. JXH acknowledges the support on software issues from Tesla Jeltema and the Fermi science support team, especially Elizabeth C. Ferrara, Jeremy S. Perkins, Dave Davis and Robin Corbet. JXH is supported by the European Commissions Framework Programme 7, through the Marie Curie Initial Training Network Cosmo-Comp (PITNGA-2009-238356), and partially supported by NSFC (10878001, 11033006, 11121062) and by the CAS/SAFEA International Partnership Program for Creative Research Teams (KJCX2-YW-T23). CSF acknowledges a Royal Society Wolfson research merit award and an ERC Advanced Investigator grant. The calculations for this work were performed on the ICC Cosmology Machine, which is part of the DiRAC Facility jointly funded by STFC, the Large Facilities Capital Fund of BIS, and Durham University. This work was supported in part by an STFC rolling grant to the ICC. The work of D.M. is supported in part from the SCOPES project IZ73Z0 128040 of Swiss National Science Foundation, grant No CM-203-2012 for young scientists of National Academy of Sciences of Ukraine, Cosmophysics programme of the National Academy of Sciences of Ukraine and by the State Programme of Implementation of Grid Technology in Ukraine.

REFERENCES

Aalseth C. E. et al., 2011a, Physical Review Letters, 106, 131301, arXiv:1002.4703

- Aalseth C. E. et al., 2011b, *Physical Review Letters*, 107, 141301, arXiv:1106.0650
- Abazajian K. N., Kaplinghat M., 2012, *Phys. Rev. D*, 86, 083511, arXiv:1207.6047
- Abdo A. A. et al., 2010, *ApJ*, 720, 435, arXiv:1003.0895
- Abdo A. A. et al., 2009, *ApJ*, 707, 55, arXiv:0910.3565
- Ackermann M. et al., 2011, *Physical Review Letters*, 107, 241302, arXiv:1108.3546
- Ackermann M. et al., 2010, *J. Cosmology Astropart. Phys.*, 5, 25, arXiv:1002.2239
- Ahmed Z., et al., 2011, *Physical Review Letters*, 106, 131302, arXiv:1011.2482
- Aleksić J. et al., 2012, *A&A*, 541, A99, arXiv:1111.5544
- Angloher G. et al., 2012, *European Physical Journal C*, 72, 1971, arXiv:1109.0702
- Aprile E., et al., 2011, *Physical Review Letters*, 107, 131302, arXiv:1104.2549
- Baxter E. J., Dodelson S., 2011, *Phys. Rev. D*, 83, 123516, arXiv:1103.5779
- Bernabei R. et al., 2010, *European Physical Journal C*, 67, 39, arXiv:1002.1028
- Bertone G., Hooper D., Silk J., 2004, *Phys. Rep.*, 405, 279
- Böhringer H., Briel U. G., Schwarz R. A., Voges W., Hartner G., Trümper J., 1994, *Nature*, 368, 828
- Boyarsky A., Malyshev D., Ruchayskiy O., 2011, *Physics Letters B*, 705, 165, arXiv:1012.5839
- Boyarsky A., Malyshev D., Ruchayskiy O., 2012, *ArXiv e-prints*, arXiv:1205.4700
- Bringmann T., Huang X., Ibarra A., Vogl S., Weniger C., 2012, *J. Cosmology Astropart. Phys.*, 7, 54, arXiv:1203.1312
- Ciafaloni P., Comelli D., Riotto A., Sala F., Strumia A., Urbano A., 2011, *J. Cosmology Astropart. Phys.*, 3, 19, arXiv:1009.0224
- Cirelli M. et al., 2011, *J. Cosmology Astropart. Phys.*, 3, 51, arXiv:1012.4515
- Collar J. I., 2011a, *ArXiv e-prints*, arXiv:1103.3481
- Collar J. I., 2011b, *ArXiv e-prints*, arXiv:1106.0653
- Dasgupta B., Laha R., 2012, *ArXiv e-prints*, arXiv:1206.1322
- Diemand J., Kuhlen M., Madau P., 2007, *ApJ*, 657, 262, arXiv:astro-ph/0611370
- Duffy A. R., Schaye J., Kay S. T., Dalla Vecchia C., 2008, *MNRAS*, 390, L64, arXiv:0804.2486
- Enßlin T., Pfrommer C., Miniati F., Subramanian K., 2011, *A&A*, 527, A99, arXiv:1008.4717
- Finkbeiner D. P., 2004, *ArXiv e-prints*, arXiv:astro-ph/0409027
- Fouqué P., Solanes J. M., Sanchis T., Balkowski C., 2001, *A&A*, 375, 770, arXiv:astro-ph/0106261
- Gao L., Frenk C. S., Jenkins A., Springel V., White S. D. M., 2012, *MNRAS*, 419, 1721, arXiv:1107.1916
- Geringer-Sameth A., Koushiappas S. M., 2011, *Physical Review Letters*, 107, 241303, arXiv:1108.2914
- Gondolo P., Silk J., 1999, *Physical Review Letters*, 83, 1719, arXiv:astro-ph/9906391
- Han J., Frenk C. S., Eke V. R., Gao L., White S. D. M., 2012, *ArXiv e-prints*, arXiv:1201.1003
- Hoffman G. L., Olson D. W., Salpeter E. E., 1980, *ApJ*, 242, 861
- Hooper D., 2012, *ArXiv e-prints*, arXiv:1201.1303
- Hooper D., Finkbeiner D. P., Dobler G., 2007, *Phys. Rev. D*, 76, 083012, arXiv:0705.3655
- Hooper D., Goodenough L., 2011, *Physics Letters B*, 697, 412, arXiv:1010.2752
- Hooper D., Linden T., 2011a, *Phys. Rev. D*, 83, 083517, arXiv:1011.4520
- Hooper D., Linden T., 2011b, *Phys. Rev. D*, 84, 123005, arXiv:1110.0006
- Huang X., Vertongen G., Weniger C., 2012, *J. Cosmology Astropart. Phys.*, 1, 42, arXiv:1110.1529
- Jeltema T. E., Kehayias J., Profumo S., 2009, *Phys. Rev. D*, 80, 023005, arXiv:0812.0597
- Jungman G., Kamionkowski M., Griest K., 1996, *Phys. Rep.*, 267, 195, arXiv:hep-ph/9506380
- Karachentsev I. D., Nasonova O. G., 2010, *MNRAS*, 405, 1075, arXiv:1002.2085
- Linden T., Hooper D., Yusef-Zadeh F., 2011, *ApJ*, 741, 95, arXiv:1106.5493
- Macías-Ramírez O., Gordon C., Brown A. M., Adams J., 2012, *Phys. Rev. D*, 86, 076004, arXiv:1207.6257
- Mattox J. R. et al., 1996, *ApJ*, 461, 396
- Nolan P. L., Abdo A. A., Ackermann M., Ajello M., Allafort A., et al., 2012, *ApJS*, 199, 31, arXiv:1108.1435
- Pinzke A., Pfrommer C., 2010, *MNRAS*, 409, 449, arXiv:1001.5023
- Pinzke A., Pfrommer C., Bergström L., 2011, *Phys. Rev. D*, 84, 123509, arXiv:1105.3240
- Schindler S., Binggeli B., Böhringer H., 1999, *A&A*, 343, 420, arXiv:astro-ph/9811464
- Smith S., 1936, *ApJ*, 83, 23
- Springel V. et al., 2008, *Nature*, 456, 73, arXiv:0809.0894
- Su M., Finkbeiner D. P., 2012, *ArXiv e-prints*, arXiv:1206.1616
- Tempel E., Hektor A., Raidal M., 2012, *J. Cosmology Astropart. Phys.*, 9, 32, arXiv:1205.1045
- Tonry J. L., Blakeslee J. P., Ajhar E. A., Dressler A., 2000, *ApJ*, 530, 625, arXiv:astro-ph/9907062
- Tully R. B., Shaya E. J., 1984, *ApJ*, 281, 31
- Urban O., Werner N., Simionescu A., Allen S. W., Böhringer H., 2011, *MNRAS*, 414, 2101, arXiv:1102.2430
- Vitale V., Morselli A., for the Fermi/LAT Collaboration, 2009, *ArXiv e-prints*, arXiv:0912.3828
- Weniger C., 2012, *J. Cosmology Astropart. Phys.*, 8, 7, arXiv:1204.2797
- Zaharijas G., Cuoco A., Yang Z., Conrad J., 2010, *ArXiv e-prints*, arXiv:1012.0588
- Zimmer S., Conrad J., for the Fermi-LAT Collaboration, Pinzke A., 2011, *ArXiv e-prints*, arXiv:1110.6863

APPENDIX A: DETECTION OF NEW POINT SOURCES

We model the new point sources assuming power-law spectra. For a given pixel, we calculate the TS value for an assumed new point source centered on that pixel. The TS calculation is performed using the binned method in the `pyLikelihood` tool, with a null model which includes the GAL and EG components and all the 2FGL sources within 15 deg of each cluster, but with the parameters of the 2FGL sources fixed. Around each cluster, we carry out a first scan

of all the pixels within the cluster virial radius (and within 4 deg around Coma) using a pixel size of 0.2 deg.

Regions with a peak $TS > 16$ are identified as potential locations of new point sources. We then scan each potential point source region using 10 times smaller pixels. The calculated TS map is then interpolated with cubic splines down to 0.002 deg/pixel. The value and location of the TS peak is taken as the TS and position for a new point source, if the peak $TS > 25$. In case several peaks are clustered, we first extract the primary TS peak, then scan for lower TS peaks by including the newly detected sources into the null model. In our sample, no secondary peaks survive this iterative examination to be identified as new point sources.

The new point sources are listed in Table A1, and plotted in Figure 1 and C1. Sources in Virgo and Fornax are prefixed by “V” and “F” in their names respectively. None of these new sources show significant variability when binned over monthly scale. The last column of Table A1 shows possible associations of astrophysical sources with these new detections, which are found to lie within the 2σ confidence region of the detections.

Table A1. Newly detected point sources

Name	TS	RA (deg)	DEC (deg)	Flux (10^{-9} ph \cdot cm $^{-2}$ s $^{-1}$)	Spectral Index ^a	Seperation (deg) ^b	Possible Association
V1	32.5	190.920	16.194	5.9 ± 1.4	-2.3 ± 0.2	4.96	LBQS 1241+1624
V2	31.8	185.698	11.116	3.7 ± 1.0	-2.0 ± 0.2	2.31	[VV2006] J122307.2+110038
V3	31.6	184.066	9.456	2.3 ± 0.8	-1.9 ± 0.2	4.58	2MASX J12160619+0929096
V4	30.5	185.894	8.286	1.6 ± 0.7	-1.8 ± 0.2	4.42	SDSS J122321.38+081435.2
F1	26.3	58.300	-36.386	0.9 ± 0.6	-1.7 ± 0.3	3.17	[VV98b] J035305.1-362308

^aPhoton spectral index β for $dN/dE \propto E^\beta$.

^bDistance to cluster centre.

APPENDIX B: MONTE-CARLO SIMULATION OF UNDETECTED POINT SOURCE POPULATIONS

To model the undetected population we adopt the following model based on the results of Abdo et al. (2010). Each point source is assumed to have a power-law spectrum defined by two parameters: flux and spectral index. The spectral index distribution is modeled as a Gaussian of mean $\mu = 2.36$ and $\sigma = 0.27$. The flux and spectral index are assumed to be independent. The differential number density of undetected point sources is assumed to be given by

$$\frac{dN}{dSd\Omega} = A\left(\frac{S}{S_b}\right)^{-\beta}. \quad (\text{B1})$$

We adopt $S_b = 6.6 \times 10^{-8}$ ph cm $^{-2}$ s $^{-1}$, $\beta = 1.58$ and $A = 4.1 \times 10^8$ cm 2 s Sr $^{-1}$, as derived from Table 4 of Abdo et al. (2010). Since the total number of point sources diverges for $\beta > 1$, we cut off the flux distribution at $S_{\min} = 1 \times 10^{-11}$ ph cm $^{-2}$ s $^{-1}$. Due to the dependence of the detection efficiency on flux and spectral shape, there is no obvious cutoff in the maximum flux of undetected sources. We take $S_{\max} = 1 \times 10^{-8}$ ph cm $^{-2}$ s $^{-1}$ as the detection threshold which corresponds to a detection completeness of $\sim 50\%$, comparing 2FGL source counts and the model. This implies an undetected point source flux of 14% of the standard EG background, consistent with the results of Abdo et al. (2010). The synthetic spectrum of these undetected point sources is then subtracted from the standard EG template to yield a residual EG template for the simulation.

We perform 750 independent realizations of the 15 deg Virgo region in the presence of undected point sources. For each realization, we generate mock data in the following steps:

- Generate a Poisson random number for the total number of undetected point sources within 15 deg.
- For each point source, generate a random spectral index and a random flux according to the distributions specified above. Also, generate random coordinates for the point source according to a uniform distribution on the sky.
- Feed these point sources and the 2FGL point sources within 15 deg, as well as the GAL and remaining EG components, to `gtobssim`.

The standard likelihood analysis is then applied to the

simulated data without including any of the randomly generated point sources in the model. Here we only consider the CR-only and the DM-only models. In Fig. B1 we show the cumulative probability distribution of TS values. Simple scaled versions of the standard $\chi^2(TS)/2$ distributions can roughly describe the TS distribution and provide the simplest way to convert the fitted TS to the standard χ^2 -distributed TS .

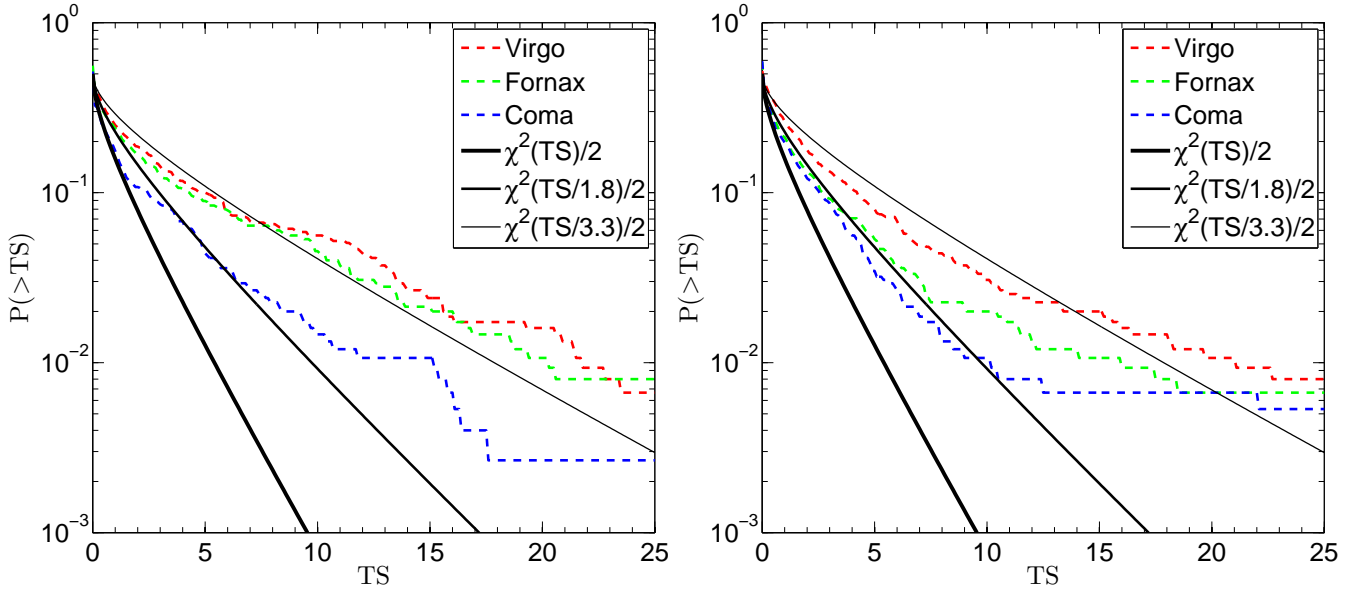


Figure B1. Distribution of TS from simulated data which include a population of undetected point sources. Left: the distribution of TS for DM-only models, where the DM particle mass is taken to be ~ 30 GeV and the DM follows the EXT cluster profile. Right: the distribution of TS for CR-only models. In each panel the dashed lines show the distribution extracted from the simulations for three cluster models and the solid lines show a rescaled version of the standard cumulative χ^2 distribution.

APPENDIX C: GAMMA-RAY IMAGES FOR COMA AND FORNAX

In this Appendix we show gamma-ray images for the Coma and Fornax cluster regions. The corresponding image for Virgo is shown in Fig. 1.

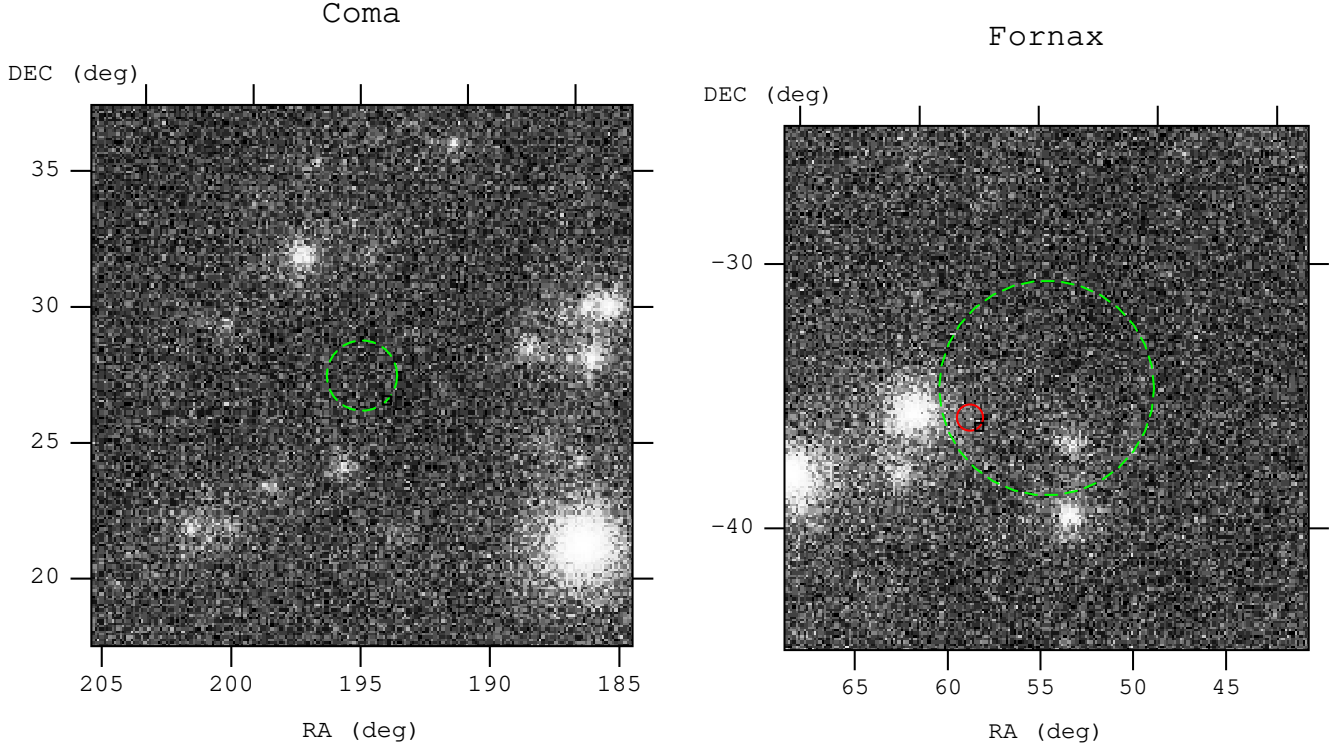


Figure C1. Integrated gamma-ray images in the Coma (left) and Fornax (right) cluster regions. The green dashed circle marks the virial radius of the cluster. Each image covers $20 \times 20 \text{ deg}^2$ with a pixel size of 0.1 deg, constructed from the 3-year Fermi-LAT data applying the data cuts described in the main text. The small solid circle in Fornax marks the position of a newly detected point source.

APPENDIX D: SEMI-ANALYTIC FORMULA FOR THE COSMIC RAY INDUCED GAMMA-RAY EMISSION

Here we summarize the relevant equations for calculating the CR induced gamma-ray emission in galaxy clusters as derived by Pinzke & Pfrommer (2010) and Pinzke et al. (2011). The CR induced photon source function from pion decay can be decomposed as:

$$\frac{dN_\gamma}{dt dV dE} = A(r) s(E).$$

The spatial part is given by:

$$A(r) = ((C_{200} - C_{centre})(1 + (\frac{r}{R_{trans}})^{-\beta})^{-1} + C_{centre}) \rho_{gas}(r)^2, \quad (\text{D1})$$

with

$$C_{centre} = 5 \times 10^{-7} \quad (\text{D2})$$

$$C_{200} = 1.7 \times 10^{-7} \times (M_{200}/10^{15} M_\odot)^{0.51} \quad (\text{D3})$$

$$R_{trans} = 0.021 R_{200} \times (M_{200}/10^{15} M_\odot)^{0.39} \quad (\text{D4})$$

$$\beta = 1.04 \times (M_{200}/10^{15} M_\odot)^{0.15} \quad (\text{D5})$$

The spectrum is given as:

$$s(E) = g(\zeta_{p,max}) D_\gamma(E_\gamma, E_{\gamma,break}) \frac{16}{3m_p^3 c} \times \sum_{i=1}^3 \frac{\sigma_{pp,i}}{\alpha_i} (\frac{m_p}{2m_{\pi^0}})^{\alpha_i} \Delta_i [(\frac{2E_\gamma}{m_{\pi^0} c^2})^{\delta_i} + (\frac{2E_\gamma}{m_{\pi^0} c^2})^{-\delta_i}]^{-\frac{\alpha_i}{\delta_i}} \quad (\text{D6})$$

with $\Delta = (0.767, 0.143, 0.0975)$, $\alpha = (2.55, 2.3, 2.15)$, $\delta_i \simeq 0.14\alpha_i^{-1.6+0.44}$. Here m_p is the proton mass, m_{π^0} the neu-

tral pion mass and c the speed of light. The maximum shock acceleration efficiency is chosen to be $\zeta_{p,max} = 0.5$ so that $g(\zeta_{p,max}) = 1$. The term $D_\gamma(E_\gamma, E_{\gamma,break})$ describes the diffusive CR losses due to escaping protons as

$$D_\gamma(E_\gamma, E_{\gamma,break}) = [1 + (\frac{E_\gamma}{E_{\gamma,break}})^3]^{-1/9}. \quad (\text{D7})$$

The proton cut-off energy is

$$E_{p,break} \approx \frac{10^8}{8} \text{ GeV} (\frac{R_{200}}{1.5 \text{ Mpc}})^6. \quad (\text{D8})$$

The energy $E_{p,break}$ is related to the photon cut-off energy, $E_{\gamma,break}$, through the momentum relation $P_\gamma \approx \frac{E_p}{8}$. The effective cross-section for proton-proton interactions is given by:

$$\sigma_{pp,i} \simeq 32(0.96 + e^{4.42-2.4\alpha_i}) \text{ mbarn}. \quad (\text{D9})$$

The gas density is fitted with multiple beta-profiles:

$$\rho_{gas} = \frac{m_p}{X_H X_e} \{ \sum_i n_i^2(0) [1 + (\frac{r}{r_{c,i}})^2]^{-3\beta_i} \}^{1/2}, \quad (\text{D10})$$

where $X_H = 0.76$ is the primordial hydrogen mass fraction and $X_e = 1.157$ is the ratio of electron and hydrogen number densities in the fully ionized intracluster medium, with parameter values for $n_i(0)$, $r_{c,i}$ and β_i listed in TABLE VI of Pinzke et al. (2011).

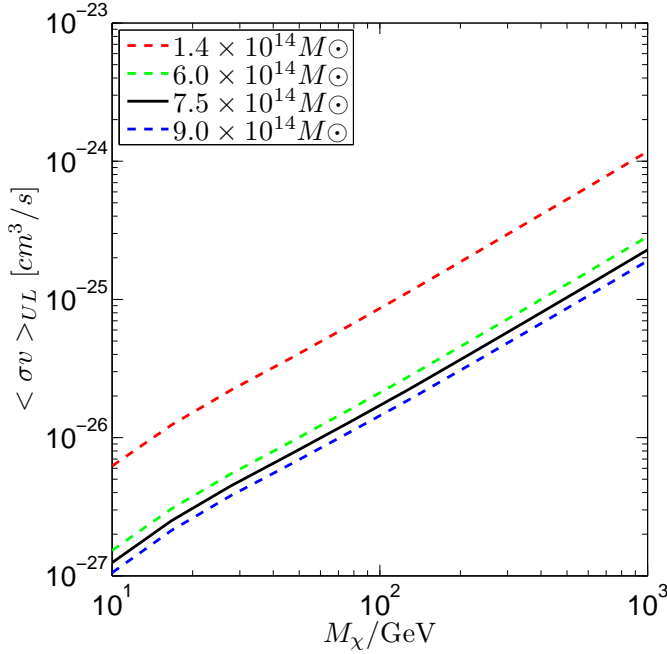


Figure E1. Upper limits on the cross-section for DM annihilating into the $b\bar{b}$ channel in the no-CR model. Different lines correspond to different adopted values for the mass of the dark matter halo of the Virgo cluster, as labelled. No allowance for undetected point sources has been made in this figure.

APPENDIX E: EFFECT OF MASS UNCERTAINTIES IN VIRGO

We adopt a virial mass for Virgo of $7.5 \pm 1.5 \times 10^{14} M_\odot$, as estimated by Tully & Shaya (1984) from an analysis of the infall pattern of galaxies around Virgo. This value is consistent with other dynamical measurements (Smith 1936; Hoffman et al. 1980; Tonry et al. 2000; Fouqué et al. 2001; Karachentsev & Nasonova 2010). Mass estimates from X-ray gas modelling tend to give somewhat lower values (Böhlinger et al. 1994; Schindler et al. 1999; Urban et al. 2011). Thus, in addition to our adopted mass uncertainty from Tully & Shaya (1984), as an extreme case, we consider also a value of $1.4 \times 10^{14} M_\odot$, obtained by scaling the X-ray estimate to the virial radius (Urban et al. 2011). In Fig. E1 we show the effect of adopting these different masses on the upper limits for DM annihilation in the $b\bar{b}$ channel. Since the flux upper limit is insensitive to slight changes in the profile shape and thus in the mass, while the luminosity (or integrated J factor) scales linearly with mass, the cross-section upper limits are expected to be roughly inversely proportional to mass. This is indeed the case in Fig. E1, where $\langle \sigma v \rangle_{UL} \propto M_{200}^{-0.9}$.